

ARTICLE

Received 24 Apr 2014 | Accepted 21 Jan 2015 | Published 2 Mar 2015

DOI: 10.1038/ncomms7334

Self-biased reconfigurable graphene stacks for terahertz plasmonics

J.S. Gomez-Diaz^{1,2}, C. Moldovan³, S. Capdevila⁴, J. Romeu⁵, L.S. Bernard⁶, A. Magrez⁷, A.M. Ionescu³
& J. Perruisseau-Carrier^{1,‡}

The gate-controllable complex conductivity of graphene offers unprecedented opportunities for reconfigurable plasmonics at terahertz and mid-infrared frequencies. However, the requirement of a gating electrode close to graphene and the single ‘control knob’ that this approach offers limits the practical implementation and performance of these devices. Here we report on graphene stacks composed of two or more graphene monolayers separated by electrically thin dielectrics and present a simple and rigorous theoretical framework for their characterization. In a first implementation, two graphene layers gate each other, thereby behaving as a controllable single equivalent layer but without any additional gating structure. Second, we show that adding an additional gate allows independent control of the complex conductivity of each layer within the stack and provides enhanced control on the stack equivalent complex conductivity. These results are very promising for the development of THz and mid-infrared plasmonic devices with enhanced performance and reconfiguration capabilities.

¹Adaptive MicroNano Wave Systems, École Polytechnique Fédérale de Lausanne (EPFL), Lausanne 1015, Switzerland. ²Department of Electrical and Computer Engineering, University of Texas at Austin, Guadalupe 1616, 1 University Station C0803, Austin, Texas 78712, USA. ³Nanoelectronics Devices Laboratory, École Polytechnique Fédérale de Lausanne (EPFL), Lausanne 1015, Switzerland. ⁴Laboratory of Electromagnetics and Acoustics (LEMA), École Polytechnique Fédérale de Lausanne, Lausanne 1015, Switzerland. ⁵AntenaLAB, Universitat Politècnica de Catalunya, C/Jordi Girona 1-3, Barcelona 08034, Spain. ⁶Laboratory of Physics and Complex Matter, École Polytechnique Fédérale de Lausanne, Lausanne 1015, Switzerland. ⁷Crystal growth facility, École Polytechnique Fédérale de Lausanne (EPFL), Lausanne 1015, Switzerland. Correspondence and requests for materials should be addressed to J.S.G.-D. (email: juan-sebastian.gomez@utexas.edu).

[‡]Deceased.

The strong graphene–light interaction has led to the rapid development of graphene plasmonics^{1,2}, which benefit from the unique electrical properties of graphene in the terahertz (THz) and mid-infrared frequency bands³. The characterization of single-layer graphene structures has already been done for microwaves^{4–7}, THz^{7–9} and optics^{3,10}, and some promising applications such as modulators^{11–16}, plasmonic waveguides^{17,18} and Faraday rotators¹⁹ have been developed. However, the simple implementation and performance of these devices might be hindered by the presence of a gating electrode located close to graphene and the relatively weak control that this approach offers over the conductivity of graphene^{11,20}. These limitations can be overcome by using graphene stacks, structures composed of two or more isolated graphene layers separated by electrically thin dielectrics, which lead to increased conductivity and may provide novel reconfiguration strategies.

Optical plasmons and quantum transport in such structures have already been studied theoretically^{21–23}, whereas some experimental studies have focused on the Anderson localization of Dirac electrons in one of the graphene layers at DC due to the screening effect^{24–26}. Furthermore, the Coulomb drag of massless fermions has been experimentally measured²⁷, while both intra- and interlayer phenomena in structures surrounded by various dielectrics and their influence in the supported in-phase and out-of-phase plasmons have also been considered^{28,29}. Potential applications of graphene stacks include modulators¹², enhanced metasurfaces³⁰, antennas³¹, or plasmonic parallel-plate waveguides^{18,32}, among many others. Experimentally, graphene stacks have recently been applied to the development of vertical field effect transistors (FET) transistors^{33,34}. In addition, the response of unbiased graphene stacks and devices at infrared frequencies has also been investigated²⁰.

In this context, our work here demonstrates the concept of reconfigurable graphene stacks for THz plasmonics and presents a simple and rigorous theoretical framework for their characterization. Although the graphene monolayers within the stack are not close enough to couple through quantum effects^{26,34}, their extremely small separation in terms of wavelength allows the stack to behave as a single equivalent layer of increased conductivity. The enhanced tunable capabilities of the proposed structure are experimentally demonstrated in different scenarios, including the mutual gating between the graphene layers and the independent control of each sheet through two different biasing gates. The measurement of the total stack conductivity σ_S for various combinations of gate voltages permits not only the extraction of the different parameters that define each of the layers but also the determination of the effective gate capacitance of the surrounding dielectrics. The proposed formulation also allows the design of structures with the desired tunable conductivity behaviour. Our results show that reconfigurable graphene stacks boost the available range of complex conductivity values provided by single-layer structures, thus facilitating the easy implementation of THz and mid-infrared plasmonic devices with enhanced reconfiguration capabilities.

Results

Operation principle of reconfigurable graphene stacks. The structure under analysis is shown in Fig. 1, where incident and transmitted beams required for THz time-domain measurements have been artistically rendered. The sample consists of two chemically vapour deposited (CVD) graphene monolayers separated by an electrically thin ($d \sim 80$ nm) polymethylmethacrylate (PMMA) layer. Metal contacts, added using optical lithography followed by the evaporation of 50 nm of gold, have been included for biasing purposes. The sample is measured in the 0.5–2.5 THz

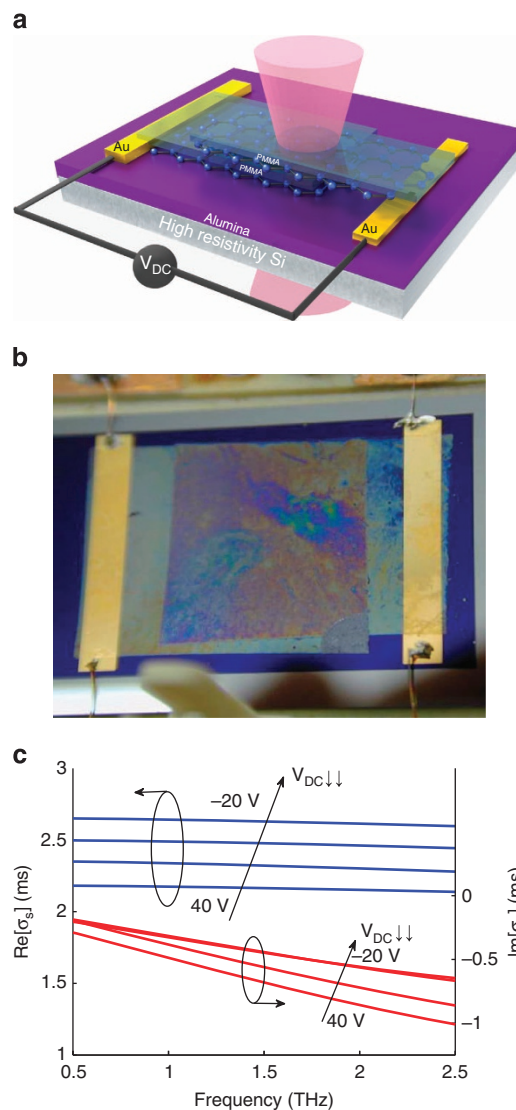


Figure 1 | Graphene stack composed of two monolayer graphene sheets separated by an electrically thin layer of PMMA. (a) Artistic rendering of the fabricated sample. Incident and transmitted beams, employed for THz time-domain measurements, are illustrated for convenience. **(b)** Picture of the fabricated device. **(c)** Gate-controlled conductivity of the stack at terahertz. Measured real (blue) and imaginary (red) components of the conductivity are plotted versus frequency. Results are shown for various voltages V_{DC} applied between the two graphene sheets of the stack.

frequency range using time-domain spectroscopy. The complex conductivity of the graphene stack is then retrieved using a dedicated formulation^{8,35,36}. Details regarding the fabrication, measurement and stack conductivity extraction process are provided in Methods. As the dielectric separation layer between the graphene layers is extremely thin in terms of wavelengths²⁰ ($d/\lambda_0 \ll 10^{-3}$), an incoming electromagnetic wave observes a stack conductivity σ_S

$$\sigma_S = \sigma_{\text{top}} + \sigma_{\text{bot}}, \quad (1)$$

where σ_{top} and σ_{bot} are the complex conductivity of the top and bottom graphene layers, respectively. Figure 1c plots the frequency-dependent real and imaginary parts of the extracted conductivity σ_S for several DC biasing voltages applied between the graphene layers. In the low THz band, the real component of the sample conductivity does not vary with frequency, whereas the magnitude of the imaginary part, which facilitates the

propagation of surface plasmons in this frequency band³⁷, increases with frequency following a standard Drude model.

Figure 2 shows the measured reconfiguration capabilities of the fabricated graphene stack at $f=1.5$ THz in different scenarios. In the first case, depicted in Fig. 2a, a gate voltage V_{DC} is applied between the two graphene layers. The results clearly confirm the tunability of σ_s and the ability of the stack to self-bias. The extracted chemical potentials corresponding to each graphene sheet, computed using the procedure detailed in Methods combined with the measured stack conductivity and further validated by Raman scattering measurements³⁸, are depicted versus the applied gate voltage in Fig. 3. Both graphene layers are p -doped and they present slightly different Fermi levels. This difference can be due to the defects induced in the graphene layers during growth or transfer³⁹ and to the influence of the surrounding dielectrics^{40–42}. In addition to the different morphology of the surrounding dielectrics, contamination during processing⁴³ and molecules absorbed from ambient air⁴⁴ play a crucial role. Applying a positive bias between the graphene sheets injects electrons/holes into the top/bottom layers, as illustrated in Supplementary Fig. 1, which in turn increases/decreases their chemical potential (or vice versa in the case of a negative applied bias). Furthermore, the extracted conductivities and chemical potentials exhibit a hysteresis behaviour, which arises due to the charges and impurities trapped in the surrounding dielectrics, as occurs in graphene transistors⁴⁵.

Another interesting possibility for controlling the stack conductivity and boost its tuning range consists of applying voltages V_1 and V_2 to the bottom and top graphene layers, as illustrated in Fig. 2b. For the sake of simplicity, we have implemented this biasing scheme by including an additional polysilicon gate below the lower graphene layer. Alternatively, this configuration might be implemented by stacking a higher number of graphene layers in the same structure. Finally, Fig. 2c presents a simple biasing procedure able to control the conductivity of each layer independently. Specifically, applying a fixed voltage V_2-V_1 between the graphene sheets fixes the chemical potential of the top layer, whereas the carrier density on the bottom layer is tuned by modifying the voltage V_1 , as will be theoretically demonstrated below. Note that a voltage $V_1=0$ V does not exactly simplify this experiment to the one of Fig. 2a, due to the weak electrostatic fields that may arise between the bottom graphene sheet and the polysilicon layers in practice (see Methods). The examples illustrated in Fig. 2 demonstrate the large potential of graphene stacks for THz plasmonics, as it is possible to control the behaviour of the different layers within a unique stack to achieve the complex conductivity required for a desired application.

Static and dynamic characteristics. The graphene stack is theoretically analysed in two different but interdependent steps. First, the carrier density on each graphene layer is determined as a function of the applied gate voltages using an electrostatic approach. Second, this information is employed to compute the frequency-dependent conductivity σ_s of the stack. In a general case of two graphene sheets biased by different gate voltages V_1 and V_2 (see inset of Fig. 2b and Supplementary Fig. 1), these carrier densities can be approximated as

$$qn_s^{\text{top}} = qn_{s_1}^{\text{top}} - C_{\text{ox}}^{\text{top}}(V_2 - V_1), \tag{2}$$

$$qn_s^{\text{bot}} = qn_{s_1}^{\text{bot}} + C_{\text{ox}}^{\text{top}}(V_2 - V_1) - C_{\text{ox}}^{\text{bot}}V_1, \tag{3}$$

where $-q$ is the electron charge, n_s^p is the total carrier density in the p graphene layer (with $p = \{\text{bottom, top}\}$), $n_{s_1}^p$ corresponds to the pre-doping of the p sheet and C_{ox}^p is the capacitance of the

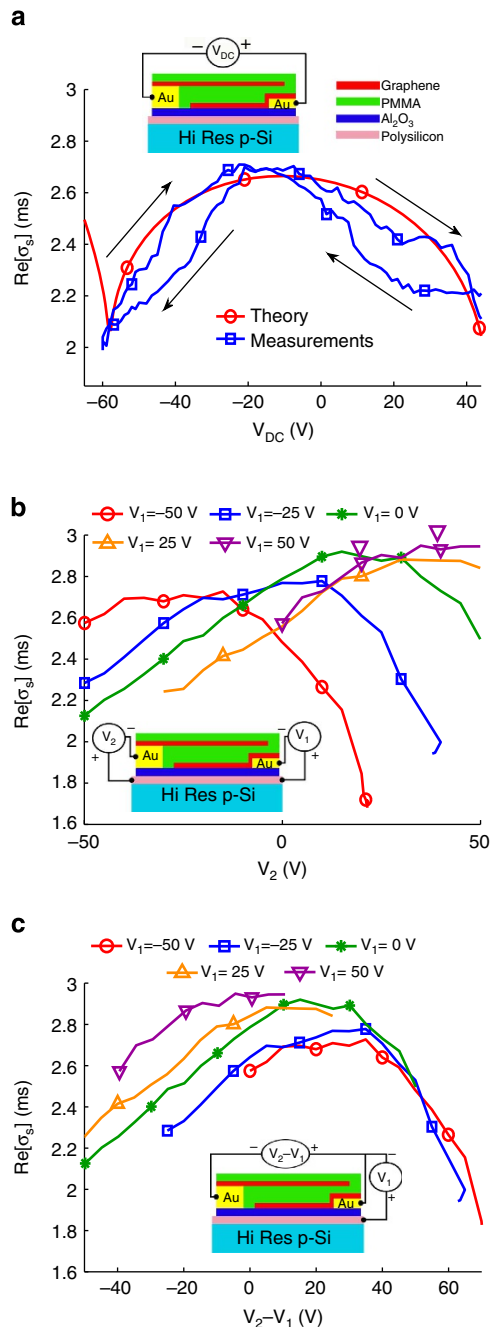


Figure 2 | Reconfiguration capabilities of the fabricated graphene stack.

(a) Measured conductivity plotted versus a voltage V_{DC} applied between the two graphene sheets. Simulated results are included for comparison purposes. (b) Measured conductivity plotted versus the voltage V_2 applied to the top graphene sheet for different values of the bottom gate voltage V_1 . (c) Measured conductivity plotted versus the voltage V_2-V_1 applied between the graphene layers for different values of the bottom gate voltage V_1 . The different insets illustrate the sample cross-section and its connection to the voltage sources. For the sake of clarity, the hysteresis behaviour of the stack conductivity has been removed in cases **b** and **c**. The operation frequency is set to $f=1.5$ THz.

p dielectric layer. Once the carrier densities are known, the Fermi level of each graphene layer and the conductivity σ_s , which determines the electromagnetic behaviour of the whole stack, can be easily computed (see Methods for details). Moreover, equations (2) and (3) further confirm that it is possible to

control the conductivity of each graphene layer independently. Specifically, the carrier density on both layers similarly depends on the difference between the applied voltages ($V_2 - V_1$), while the bottom layer additionally depends on the voltage V_1 . Consequently, modifying the voltage V_1 while keeping constant the difference $V_2 - V_1$ allows the independent control of each layer's conductivity.

This simple framework allows a rigorous extraction of the characteristics of the stack from the measured data, including the relaxation time (τ_p) and the Fermi level (μ_c^p) of the graphene

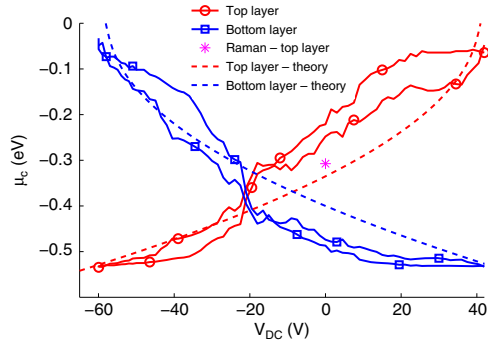


Figure 3 | Extracting the chemical potentials of the two layers composing the graphene stack. Results are computed versus the applied gate voltage V_{DC} (see inset of Fig. 2a), as detailed in Methods. Additional results obtained by measuring the dopants of the top layer using a Raman scattering technique³⁸ (at $V_{DC} = 0$ V) and by the proposed theory are included for comparison purposes.

layers and the capacitance (C_{ox}^{CP}) of the surrounding dielectrics. This procedure, detailed in Methods, relies on applying different sets of gate voltages to the sample to measure various stack conditions, which in turns allows independent extraction of all of the aforementioned parameters. A system of nonlinear coupled equations is then imposed, relating the measured data to the theoretical characteristics of the stack. In the particular case of the sample shown in Fig. 2a, the solution of the system of equations yields $\tau_{top} = 0.033$ ps, $\tau_{bot} = 0.03$ ps, $\mu_c^{top} = -0.4$ eV and $\mu_c^{bot} = -0.355$ eV, whereas the gate capacitance of the PMMA separation layer is $C_{ox}^{top} = 3.2 \cdot 10^{-4}$ F m⁻². These values are in good agreement with the measured characteristics of a single-layer graphene transferred onto a similar dielectric ($\tau = 0.029$ ps and $\mu_c = -0.425$ eV, as shown in the Supplementary Figs 2–4) and with the gate capacitance obtained using the approximate parallel-plate formula $C_{ox}^{top} = \frac{\epsilon_0 \epsilon_r}{d} \approx 3.315 \cdot 10^{-4}$ F m⁻². The simulated results, plotted in Fig. 2a and Fig. 3 together with measured data, confirm the accuracy of both the extraction procedure and the proposed model to characterize reconfigurable graphene stacks. The measured hysteresis behaviour of the sample conductivity, which is mainly related to the charges trapped in the dielectrics surrounding the graphene layers⁴⁵, is not considered in the model. In addition, the extracted values permit estimating a modulation speed of 6.2 kHz for the stack (see Supplementary Note 1), similar to the one found in single-layer graphene structures^{12,46}.

This framework can be further employed to forecast the reconfiguration capabilities of a wide variety of graphene stacks, allowing the design of structures with desired plasmonic properties and tunable behaviour. Figure 4 illustrates at $f = 1.5$ THz the real and imaginary conductivity components of a stack composed

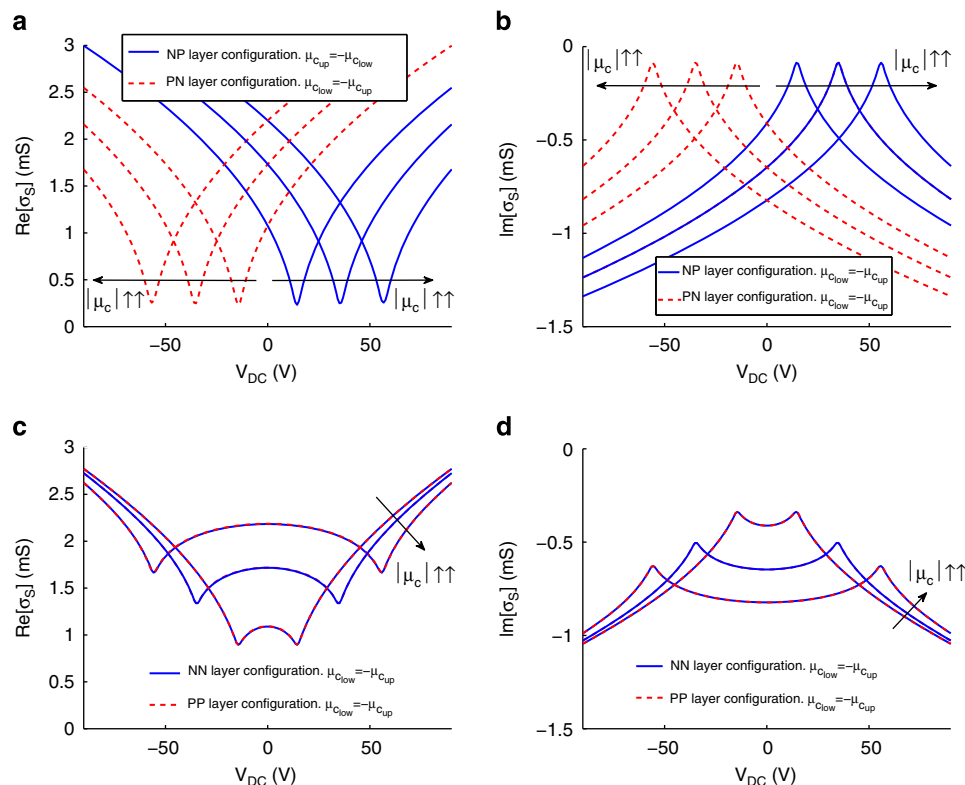


Figure 4 | Theoretical reconfiguration capabilities of various graphene stacks. Results are computed versus the type of doping of the stacks composing layers. A biasing voltage V_{DC} is applied between the graphene sheets, as illustrated in the inset of Fig. 2a. The type of doping of the layers follows the nomenclature TB , where $T = \{N, P\}$ and $B = \{N, P\}$ are related to the top and bottom layers, respectively, and $\{N, P\}$ refers to n -doped or p -doped graphene. The upper row shows the real (a) and imaginary (b) conductivity components of a stack composed of layers with opposite Fermi level. (c,d) Similar results for the case of a stack composed of layers with equal Fermi level. Other parameters are $f = 1.5$ THz, $\tau_{top} = \tau_{bot} = 0.03$ ps and $T = 300$ K.

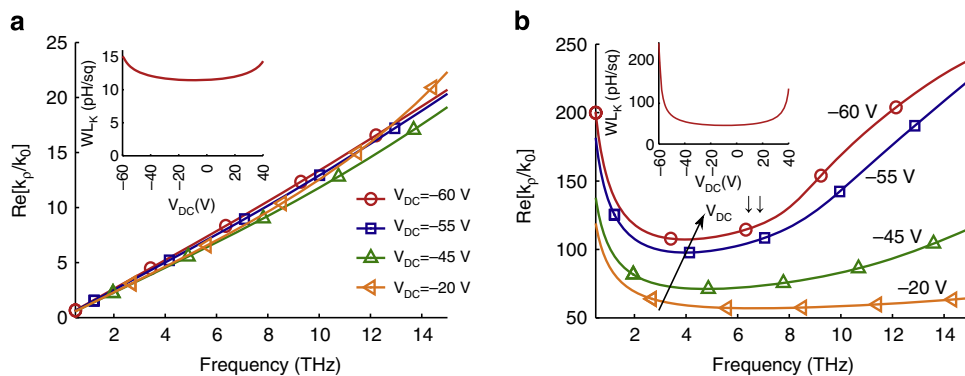


Figure 5 | Characteristics of the surface plasmons supported by the fabricated graphene stack. Results are shown for several values of the voltage V_{DC} applied between the two graphene sheets of the stack (see inset of Fig. 2a). **(a)** TM mode. **(b)** Quasi TEM mode. The insets show the kinetic inductance associated to each mode versus the applied bias assuming a width $W = 10 \mu\text{m}$. Simulations (see Methods) are performed using the extracted characteristics of the stack as input parameters.

by two graphene sheets with various Fermi levels versus the gate voltage applied between the layers (see inset of Fig. 2a). Let us first consider, for simplicity, a stack where the graphene layers have a different type of doping, that is, one sheet is *p*-doped and the other is *n*-doped. In this particular case, illustrated in Fig. 4a,b, the carriers injected by the voltage source alter the carrier density on each layer in a similar way, that is, simultaneously increasing/decreasing their $|\mu_c^p|$, while keeping their opposite doping nature [$\text{sign}(\mu_c^{\text{top}}) \neq \text{sign}(\mu_c^{\text{bot}})$]. As a result, the stack conductivity is approximately twice the conductivity of an individual layer. The behaviour of the stack conductivity differs with respect to the previous case when the layers have the same type of doping, that is, if they are both *p*-doped or *n*-doped. In this case, shown in Fig. 4c,d, the carriers injected by the source modify the carrier density on each graphene sheet in an opposite direction, that is, increasing $|\mu_c|$ of one layer while reducing it on the other layer. Consequently, the stack conductivity presents a symmetrical behaviour for positive and negative gate voltages, exhibiting points of minimum conductivity in both cases. The results shown in Fig. 4 confirm that in graphene stacks, (i) the imaginary component of σ_S can be double than the one of a single-layer structure, while avoiding the presence of metallic bias, and (ii) the tuning range is significantly boosted for similar applied voltages values. In addition, the conductivity of graphene stacks can be controlled further by considering two different gate sources, as shown in the inset of Fig. 2b. Similar to the previous case, the tunable behaviour of the stack conductivity will strongly depend on the initial level and the type of doping of each graphene layer, leading to a wide variety of scenarios and reconfiguration possibilities (see Supplementary Figs 5–9).

Surface plasmons supported by graphene stacks. The measured characteristics of the fabricated stack allows to simulate the frequency-dependent properties of the surface plasmons supported by the device. Specifically, the structure supports two different modes^{32,47} (see Methods): an even transverse magnetic (TM) and an odd quasi transverse electromagnetic (TEM). The former can easily be seen as a usual TM plasmon propagating along a single-layer graphene sheet, with a conductivity equal to the stack conductivity σ_S . Figure 5a illustrates the characteristics of this mode, which presents lower-field confinement and reduced tunability compared with plasmons in single-layer graphene. This behaviour arises due to the increased imaginary component of the stack conductivity, which in turn reduces the kinetic inductance associated to this mode. The later is a perturbation of the TEM mode found in standard parallel-plate

waveguides with two perfect electric conductors. Figure 5b confirms that this mode presents remarkable characteristics in terms of field confinement and tunability, clearly outperforming single-layer graphene structures. Note that the high losses associated to CVD graphene⁴⁸, which prevent the propagation of the supported plasmons along many wavelengths, can be significantly mitigated by employing high-quality graphene in the stack⁴⁹. Supplementary Note 2 includes a comparison of the characteristics of plasmons supported by the stack and a single-layer graphene structure, and further discusses the influence of losses in both cases.

Discussion

This theoretical and experimental study of graphene stacks has demonstrated that the available range of complex conductivities in graphene stacks can be significantly boosted by two different approaches as follows: (i) mutually biasing the graphene sheets without requiring the presence of any metallic bias and (ii) including a third gate source to control the conductivity of each layer independently. The development of graphene stacks for THz plasmonic also faces some important challenges from the technological point of view, as it would be desirable to independently control the doping nature of each layer while decreasing the separation distance between the graphene sheets, to further enhance the reconfiguration possibilities of the stack. Furthermore, interlayer Coulomb effects^{28,29} should be rigorously taken into account in stacks with very small (approximately nanometres) separation distances between their layers. In addition, it would be also interesting to extend the concept of reconfigurable stacks to an arbitrarily large number of layers. The exotic characteristics of graphene stacks paves the way towards the development of a low-dimensional plasmonic platform with enhanced performance and reconfiguration capabilities. For instance, graphene stacks are the building block of the recently proposed tunable bulk hyperbolic metamaterials⁵⁰, whereas it has also demonstrated that they are able to boost the spontaneous emission of emitters⁵¹ much further than the usual monolayer graphene structures¹. In a different context, the large range of imaginary conductivity values provided by the stacks can easily be exploited in planar hyperlenses. Currently, graphene-based hyperlenses⁵² are based on achieving large contrast of conductivities within the surface by using non-uniform metallic gates located very close to graphene. However, these gates are difficult to fabricate and impair the performance of the lenses. This device could easily be implemented by a patterned graphene stack, simultaneously solving the problems related to the limited

values of the imaginary conductivity and the presence of the non-uniform metallic gate. Finally, it is noteworthy that the aforementioned features of graphene stacks can also be applied to develop improved devices such as modulators, isolators, sensors or antennas in the THz and infrared frequency bands.

Methods

Fabrication of single-layer and stack graphene structures. The samples were fabricated using CVD graphene grown on Cu foil and transferred onto the substrate using the standard wet transfer method⁵³. Supplementary Fig. 10 shows the flow of the fabrication process for the double-layer graphene stack. We deposit 72 nm of Al₂O₃ by atomic layer deposition (ALD) on an ultrahigh-resistivity (> 10 kΩ) p-type Si wafer. The ALD is performed at 200 °C using trimethylaluminum and distilled water as the reaction precursors. Before the dielectric deposition, the native oxide is removed from the Si wafer with a buffered oxide etch. The metal electrodes are patterned by optical lithography followed by a deposition of 5 nm of chromium, 50 nm of gold and a lift-off process. A graphene sheet is then transferred onto the top of one of the metal contacts. In the double-layer graphene stack, the PMMA layer used as a support polymer during the transfer process is kept on top of the graphene to act as a dielectric between the two graphene sheets. The second graphene monolayer is subsequently transferred onto the top of the other predefined metal contact, thus obtaining the final structure shown in Supplementary Fig. 10d.

The Raman spectra of the graphene employed in our devices is shown in Supplementary Fig. 11. The G and 2D band points are located at 1,589 and 2,682 cm⁻¹ with a full width at half maximum of 18 and 32 cm⁻¹, respectively. The intensity ratio of the 2D to the G band and of the D to the G band are 5.5 and 0.09, respectively. All of these numbers are typical hallmarks of monolayer graphene⁵⁴. The use of spin-coated PMMA as a separation layer between the graphene sheets allows the avoidance of problems associated with standard dielectric deposition techniques such as evaporation, sputtering⁵⁵ and ALD of oxides, which can induce defects in graphene. This approach is convenient for fabricating graphene stacks, allowing viable biasing schemes without the need of post processing the graphene. It is noteworthy that the DC isolation between the two graphene layers of the fabricated stack is not perfect, and some leakage current has been measured. However, it does not hinder the performance of the stack, as (i) the device does not operate at DC but in the THz band; and (ii) the graphene field's effect control is preserved, as the DC biasing voltage source is able to provide the required bias voltage, hence the required electrical field, even when some leakage current occurs.

In addition, note that monolayer graphene devices have been annealed in a N₂ atmosphere at 200 °C during 4 h (ref. 56). The annealing aims removing possible graphene contamination by polymer residues and other impurities⁵⁷. However, this process has not been applied to the graphene stack samples, because it would remove the PMMA layer that isolates the two graphene sheets.

THz time-domain measurements. The measurements at THz frequencies were performed using a commercial Time Domain Spectrometer (Menlo TERA-K8), which consists of a pulsed femtosecond laser at 780 nm with a pulse repetition rate of 100 MHz and a pulse width around 110 fs, offering with the current experimental setup a signal-to-noise ratio of 40 dB up to 2.5 THz. Two photoconductive antennas based on LT GaAs (Tera8-1) are used to generate and detect the THz radiation. A set of lenses focuses the THz beam onto the sample under measurement. The total sample area illuminated by the beam is around 2 mm², thus averaging graphene's features (see Supplementary Note 3). Supplementary Fig. 12 presents a schematic view of the experimental setup, with the disposition of the samples and voltage sources.

The gating was applied using a four-channel DC voltage source, Agilent N6700B. Only two channels were used for the measurements and each channel was connected to a different gold contact corresponding to a graphene layer, whereas they both shared a common ground gold contact. For safety reasons and to prevent damaging the graphene stack, the maximum voltage (taking into account both sources) was limited to ±75 V. The sample was placed on an X-Y linear stage perpendicular to the THz beam and everything was placed inside a sealed case purged with N₂ to keep a constant atmosphere during the duration of the measurements.

Stack conductivity extraction. The stack conductivity σ_s is extracted from the THz time-domain measurements, using standard thin-film characterization techniques^{8,35,36,58}. This approach is valid here, thanks to the extreme fineness of the stack in terms of wavelength ($d/\lambda \ll 10^{-3}$). An example of the different set of measured pulses employed for the extraction procedure is shown in Supplementary Fig. 13. To keep the higher possible signal-to-noise ratio, we have considered only the first transmitted pulse through the sample. Additional transmitted pulses that arise due to the internal reflections of the THz beam within the layers of the sample are clearly identified, thanks to their temporal delay, and subsequently removed.

The graphene stack is not free standing, but on top of a thick dielectric structure. Consequently, the influence of the dielectrics must be rigorously

removed to extract the actual stack conductivity. This procedure has been performed as follows: (i) a pulse is transmitted without the presence of any sample to measure and store the response (including atmosphere and possible impurities) of the sealed cage. (ii) A pulse is transmitted through an area of the sample free of graphene, which remains bare. The combination of this measured pulse with the pulse obtained in the previous step allows the extraction of the permittivity, loss tangent and thickness of the dielectrics using standard techniques^{36,58}. (iii) A pulse is transmitted through the graphene stack sample. Combining this measured pulse with the previous information, it is indeed possible to extract the conductivity of the graphene stack rigorously removing the influence of the dielectrics and surrounding atmosphere^{8,35,36}.

Graphene stack theory. The frequency-dependent conductivity σ of a single graphene layer is modelled using the Kubo formalism⁵⁹ as

$$\sigma(\omega, \mu_c, \Gamma, T) = \frac{iq^2(\omega - i2\Gamma)}{\pi\hbar^2} \left[\frac{1}{(\omega - i2\Gamma)^2} \int_0^\infty \epsilon \left(\frac{\partial f_d(\epsilon)}{\partial \epsilon} - \frac{\partial f_d(-\epsilon)}{\partial \epsilon} \right) \partial \epsilon - \int_0^\infty \frac{f_d(-\epsilon) - f_d(\epsilon)}{(\omega - i2\Gamma)^2 - 4(\epsilon/\hbar)^2} \partial \epsilon \right], \quad (4)$$

where ω is the radian frequency, ϵ is energy, $\Gamma = 1/(2\tau)$ is a phenomenological electron scattering rate assumed independent of energy, τ is the electron relaxation time, T is temperature, $-q$ is the charge of an electron, \hbar is the reduced Planck's constant and f_d is the Fermi-Dirac distribution defined as

$$f_d(\epsilon) = \left(e^{(\epsilon - \mu_c)/k_B T} + 1 \right)^{-1}, \quad (5)$$

μ_c being the chemical potential and k_B the Boltzmann's constant. This model results from the long wavelength limit of the bosonic momentum ($k_{\parallel} \rightarrow 0$) and takes into account both intraband and interband contributions of the graphene conductivity, as well as a finite temperature.

In addition, the carrier density n_s and chemical potential of the graphene layer are related through

$$n_s = n_{s_e} - n_{s_h} = \frac{2\text{sign}(\mu_c)}{\pi\hbar^2 v_f^2} \int_0^\infty \epsilon [f_d(\epsilon - \mu_c) - f_d(\epsilon + \mu_c)] \partial \epsilon, \quad (6)$$

where n_{s_e} and n_{s_h} are the electron and hole densities, respectively, ϵ is the energy and v_f is the Fermi velocity ($\sim 10^8$ cm s⁻¹ in graphene).

Let us consider the case of two graphene layers closely located within a stack, as depicted in Supplementary Fig. 1. As previously stated, the structure is analysed first by using an electrostatic approach, which determines the carrier density on the graphene layer, and then obtaining the electromagnetic behaviour of the stack at THz. Following the superposition principle (see Supplementary Fig. 1b), the carrier density on each layer are computed using equations (2) and (3). Note that this electrostatic approach approximates both graphene and polysilicon for infinite perfect conductors, to compute the carrier density on each layer. Consequently, it cannot predict the presence of weak electrostatic fields that may arise due to (i) the different DC conductivities that graphene and polysilicon present in practice and (ii) fringing effects at graphene borders. Combining these expressions with equation (6) permits the chemical potential on each graphene layer to be determined. Once these potentials are known, the frequency-dependent complex conductivity of the individual graphene sheets is retrieved using equation (4), thus allowing the total graphene stack conductivity to be computed using equation (1). Note that in this approach we have neglected (i) the influence of the separation layer located between the graphene sheets, which is electrically very small in the THz frequency range, and (ii) the possible influence of the quantum capacitance⁶⁰, which may be significant in the case of high permittivity or extremely thin (approximately nanometres) dielectrics but is completely negligible here.

It is noteworthy that the proposed approach approximates graphene's relaxation time as a constant quantity in each layer and embeds all variations of graphene conductivity versus the applied bias in the chemical potential^{7,8,61}. However, rigorous approaches indicate that the relaxation time not only depends on the defects in graphene (τ_{gr}) but also on the thermally excited surface polar phonons that may arise at the interface between graphene and the substrate (τ_{sb}), and on the frequency-dependent electron-phonon coupling (τ_{e-ph})⁶². These values are related through the Matthiessen's rule⁶³ by $\tau^{-1} = \tau_{gr}^{-1} + \tau_{sb}^{-1} + \tau_{e-ph}^{-1}$. In addition, graphene relaxation time and chemical potential are not totally independent⁶². In our particular experiments, the extracted relaxation times are very similar. As the operation frequency is in the low THz range, well below the graphene optical phonon frequency⁶², we expect that the electron-phonon phenomenon does not have an impact on the τ decay mechanism. The similarities among the extracted relaxation times, which correspond to graphene layers surrounded by different substrates, suggests that the graphene/dielectric interface provides a high τ_{sb} , thus graphene impurities and non-idealities (τ_{gr}) being the main mechanism limiting the relaxation time, that is $\tau \approx \tau_{gr}$. Other possible effects such as carrier scattering by ionized impurities⁶⁴ and the electron-hole puddle effect⁶⁵ might also modify the measured relaxation time.

Extracting the characteristics of each graphene layer. Let us consider a stack composed of two graphene layers, which are biased by two different gate sources as

depicted in Supplementary Fig. 1. The availability of the total stack conductivity σ_s for various combinations of gate voltages not only permits the extraction of the different parameters, which define each of the layers, but also determines the effective gate capacitance of the surrounding dielectrics. Specifically, given a measured stack conductivity σ_s^i obtained by applying a set i of gating voltages (V_1^i, V_2^i), equation (1) holds. This equation relies on the top and bottom complex conductivities of the layers ($\sigma_{\text{top}}^i, \sigma_{\text{bot}}^i$), which are computed using the Kubo formula of equation (4) and depend on their relaxation time ($\tau_{\text{top}}^i, \tau_{\text{bot}}^i$), Fermi levels ($\mu_c^{\text{top}}, \mu_c^{\text{bot}}$), gate capacitance of the surrounding media ($C_{\text{ox}}^{\text{top}}, C_{\text{ox}}^{\text{bot}}$) and the applied gate voltages. Considering a set of N measured stack conductivity values, obtained by applying different gate voltages, permits the extension of equation (1) into a set of nonlinear coupled equations. The numerical solution of this system of equations determines both the characteristics of each graphene layer within the stack and the gate capacitance of the surrounding media. The solution of these equations may differ slightly as a function of the measured conductivity data employed as an input. These small variations are related to diverse factors, including the hysteresis of the stack conductivity⁴⁵ or the possible change in the environmental conditions⁶⁶ (especially humidity) during the measurements. To take them into account, the various parameters extracted from all possible combination of gate voltages are finally averaged. Employing a curve fitting approach is not straightforward here, as this would involve fitting six independent variables, which could lead to non-physical parameter values and complicated post-processing steps.

Surface plasmons supported by a graphene stack. The dispersion relation of the plasmonic modes supported by a graphene stack can be computed as⁴⁷

$$(c_{\text{top}} + c_{\text{bot}}) \cos(k_z d) + i(c_{\text{top}} c_{\text{bot}} + 1) \sin(k_z d) = 0 \quad (7)$$

where

$$c_{\text{top}} = \left(\frac{\epsilon_2 k_{z1}}{\epsilon_1 k_{z2}} \right) \left(1 + \frac{\sigma_{\text{top}} k_{z1}}{\omega \epsilon_1 \epsilon_0} \right)^{-1}, \quad (8)$$

$$c_{\text{bot}} = \left(\frac{\epsilon_2 k_{z3}}{\epsilon_3 k_{z2}} \right) \left(1 + \frac{\sigma_{\text{bot}} k_{z3}}{\omega \epsilon_3 \epsilon_0} \right)^{-1}, \quad (9)$$

$k_z^2 = k_x^2 - k_y^2$, z is the direction normal to the structure and the subscript $i = 1, 2, 3$ refers to the top (air), inner (PMMA) and bottom (Al_2O_3) dielectrics. In addition, k_i denotes the wavenumber of the medium i and $k_p = \beta - j\alpha$ is the complex wavenumber of the propagating plasmon. Note that we impose $\text{Im}[k_{z(1,2)}] < 0$, to fulfill Sommerfeld's radiation condition and we assume that the stack width W is much larger than the guided wavelength (that is, $W \gg 1/k_p$). The supported even TM and odd quasi-TEM modes described by this dispersion relation can be accurately modelled using per-unit-length equivalent circuits^{32,49,67} (see Supplementary Note 2).

References

- Koppens, F. H., Chang, D. E. & de Abajo, F. J. G. Graphene plasmonics: a platform for strong light-matter interactions. *Nano Lett.* **11**, 3370–3377 (2011).
- Grigorenko, A. N., Polini, M. & Novoselov, K. S. Graphene plasmonics. *Nat. Photon.* **6**, 749–758 (2012).
- Geim, K. Graphene: status and prospects. *Science* **324**, 1530–1532 (2009).
- Hao, L. *et al.* Microwave surface impedance measurements on reduced graphene oxide. *Nanotechnology* **23**, 285706 (2012).
- Gómez-Díaz, J. S., Perruisseau-Carrier, J., Sarma, P. & Ionescu, A. Non-contact characterization of graphene surface impedance at micro and millimeter waves. *J. Appl. Phys.* **111**, 114908 (2012).
- Katsounaros, A., Cole, M. T., Tuncer, H. M., Milne, W. I. & Hao, Y. Near-field characterization of chemical vapor deposition graphene in the microwave regime. *Appl. Phys. Lett.* **102**, 233104 (2013).
- Liang, M. & Xin, H. Microwave to terahertz: characterization of carbon-based nanomaterials. *IEEE Microw. Mag.* **15**, 40–51 (2014).
- Ren, L. *et al.* Terahertz and infrared spectroscopy of gated large-area graphene. *Nano Lett.* **12**, 3711–3715 (2012).
- Buron, J. D. *et al.* Graphene conductance uniformity mapping. *Nano Lett.* **12**, 5074–5081 (2012).
- Bao, Q. & Loh, K. P. Graphene photonics, plasmonics, and broadband optoelectronic devices. *ACS Nano* **6**, 3677–3694 (2012).
- Ju, L. *et al.* Graphene plasmonics for tunable terahertz metamaterials. *Nat. Nanotechnol.* **6**, 630 (2011).
- Sensale-Rodriguez, B. *et al.* Broadband graphene terahertz modulators enabled by intraband transitions. *Nat. Commun.* **3**, 780 (2012).
- Sensale-Rodriguez, B. *et al.* Extraordinary control of terahertz beam reflectance in graphene electro-absorption modulators. *Nano Lett.* **12**, 4518–4522 (2012).
- Valmorra, F. *et al.* Low-bias active control of terahertz waves by coupling large-area cvd graphene to a terahertz metamaterial. *Nano Lett.* **13**, 3193–3198 (2013).
- Deg'Innocenti, R. *et al.* Low-bias terahertz amplitude modulator based on split-ring resonators and graphene. *ACS Nano* **8**, 2548–2554 (2014).
- Lee, S. H. *et al.* Switching terahertz waves with gate-controlled active graphene metamaterials. *Nat. Mater.* **11**, 936–941 (2012).
- Kim, J. T. & Choi, S. Y. Graphene-based plasmonic waveguides for photonic integrated circuits. *Opt. Express* **19**, 24 557–24 562 (2011).
- Christensen, J., Manjavacas, A., Thongrattanasiri, S., Koppens, F. H. L. & de Abajo, F. J. G. Graphene plasmon waveguiding and hybridization in individual and paired nanoribbons. *ACS Nano* **6**, 431–440 (2012).
- Crassee, I. *et al.* Giant faraday rotation in single and multilayer graphene. *Nat. Phys.* **7**, 48–51 (2010).
- Yan, H. *et al.* Tunable infrared plasmonic devices using graphene/insulator stacks. *Nat. Nanotechnol.* **7**, 330 (2012).
- Kechedzhi, K., Hwang, E. H. & Sarma, S. D. Gate-tunable quantum transport in double-layer graphene. *Phys. Rev. B* **86**, 165442 (2012).
- Stauber, T. & Gomez-Santos, G. Plasmons and near field amplification in double-layer graphene. *Phys. Rev. B* **85**, 075410 (2012).
- Zhu, J. J., Badalyan, S. M. & Peeters, F. M. Plasmonic excitations in coulomb-coupled n -layer graphene structures. *Phys. Rev. B* **87**, 085401 (2013).
- Ponomarenko, L. A. *et al.* Tunable metal-insulator transition in double-layer graphene heterostructures. *Nat. Phys.* **7**, 958–961 (2011).
- Gorbachev, R. V. *et al.* Strong coulomb drag and broken symmetry in double-layer graphene. *Nat. Phys.* **85**, 075410 (2012).
- Jr, J. V. *et al.* Quantum transport in double-gated graphene devices. *Solid State Commun.* **152**, 1301–1305 (2012).
- Kim, S. *et al.* Coulomb drag of massless fermions in graphene. *Phys. Rev. B* **83**, 161401 (2011).
- Badalyan, S. M. & Peeters, F. M. Effect of nonhomogenous dielectric background on the plasmon modes in graphene double-layer structures at finite temperatures. *Phys. Rev. B* **85**, 195444 (2012).
- Fischetti, M. V. Depression of the normal-superfluid transition temperature in gated bilayer graphene. *J. Appl. Phys.* **115**, 163711 (2014).
- Fallahi, A. & Perruisseau-Carrier, J. Design of tunable biperiodic graphene metasurfaces. *Phys. Rev. B* **86**, 195408 (2012).
- Tamagnone, M., Gómez-Díaz, J. S., Mosig, J. R. & Perruisseau-Carrier, J. Reconfigurable THz plasmonic antenna concept using a graphene stack. *Appl. Phys. Lett.* **101**, 214102 (2012).
- Correas-Serrano, D., Gomez-Diaz, J. S., Perruisseau-Carrier, J. & Alvarez-Melcon, A. Spatially dispersive graphene single and parallel plate waveguides: analysis and circuit models. *IEEE Trans. Microw. Theory Tech.* **61**, 4333–4344 (2013).
- Schmidt, H. *et al.* Tunable graphene system with two decoupled monolayers. *Appl. Phys. Lett.* **93**, 172108 (2008).
- Britnell, L. *et al.* Field-effect tunneling transistor based on vertical graphene heterostructures. *Science* **335**, 947–950 (2012).
- Crassee, I. *et al.* Intrinsic terahertz plasmons and magnetoplasmons in large scale monolayer graphene. *Nano Lett.* **12**, 2470–2474 (2012).
- Naftaly, M. & Miles, R. E. Terahertz time-domain spectroscopy for material characterization. *Proc. IEEE* **95**, 1658–1665 (2007).
- Hanson, G. W. Dyadic green's functions and guided surface waves for a surface conductivity of graphene. *J. Appl. Phys.* **103**, 06430 (2008).
- Das, A. *et al.* Monitoring dopants by raman scattering in an electrochemically top-gated graphene transistor. *Nat. Nanotechnol.* **3**, 210–215 (2008).
- Banhart, F., Kotakoski, J. & Krasheninnikov, A. V. Structural defects in graphene. *ACS Nano* **5**, 26–41 (2011).
- Jang, C. *et al.* Tuning the effective fine structure constant in graphene: opposing effects of dielectric screening on short- and long-range potential scattering. *Phys. Rev. Lett.* **101**, 146805 (2008).
- Konar, A., Fang, T. & Jena, D. Effect of high-k gate dielectrics on charge transport in graphene-based field effect transistors. *Phys. Rev. Lett.* **82**, 11545 (2011).
- Sharma, P., Perruisseau-Carrier, J., Moldovan, C. & Ionescu, A. M. Electromagnetic performance of rf nms graphene capacitive switches. *IEEE Trans. Nanotechnol.* **13**, 70–79 (2014).
- Ishigami, M., Chen, J. H., Cullen, W. G., Fuhrer, M. S. & Williams, E. D. Atomic structure of graphene on SiO₂. *Nano Lett.* **7**, 1643 (2007).
- Schedin, F. *et al.* Detection of individual gas molecules adsorbed on graphene. *Nat. Mater.* **6**, 652–655 (2007).
- Wang, H., Wu, Y., Cong, C., Shang, J. & Yu, T. Hysteresis of electronic transport in graphene transistors. *ACS Nano* **4**, 7221–7228 (2010).
- Sensale-Rodriguez, B. *et al.* Terahertz imaging employing graphene modulator arrays. *Opt. Exp.* **21**, 2324–2330 (2013).
- Hanson, G. W. Quasi-transverse electromagnetic modes supported by a graphene parallel-plate waveguide. *J. Appl. Phys.* **104**, 084314 (2008).
- Song, H. S. *et al.* Origin of the relatively low transport mobility of graphene grown through chemical vapor deposition. *Sci. Rep.* **2**, 337 (2012).
- Yoon, H. *et al.* Measurement of collective dynamical mass of dirac fermions in graphene. *Nat. Nanotechnol.* **9**, 594–599 (2014).

50. Othman, M. A. K., Guclu, C. & Capolino, F. Graphene-based tunable hyperbolic metamaterials and enhanced near-field absorption. *Opt. Exp.* **21**, 7614–7632 (2013).
51. Zhang, L., Fu, X., Zhang, M. & Yang, J. Spontaneous emission in paired graphene plasmonic waveguide structures. *Opt. Exp.* **21**, 7897 (2013).
52. Forati, E., Hanson, G., Yakovlev, A. & Alù, A. Planar hyperlens based on a modulated graphene monolayer. *Phys. Rev. B* **89**, 081410 (2014).
53. Reina, A. *et al.* Transferring and identification of single- and few-layer graphene on arbitrary substrates. *J. Phys. Chem. C* **112**, 17 741–17 744 (2008).
54. Ferrari, A. C. *et al.* Raman spectrum of graphene and graphene layers. *Phys. Rev. Lett.* **97**, 187401 (2006).
55. Lemme, M. C., Echtermeyer, T. J., Baus, M. & Kurz, H. A graphene field-effect device. *IEEE Electron Device Lett.* **28**, 282–284 (2007).
56. Xueshen, W., Jinjin, L., Qing, Z., Yuan, Z. & Mengke, Z. Thermal annealing of exfoliated graphene. *J. Nanomater.* **2013**, 101765 (2013).
57. Lin, Y. *et al.* Graphene annealing: how clean can it be? *Nano Lett.* **12**, 414–419 (2012).
58. Nuss, M. & Orenstein, J. in *Millimeter and Submillimeter Wave Spectroscopy of Solids* 74, 7–50 (Topics in Applied Physics, 1998).
59. Gusynin, V. P., Sharapov, S. G. & Carbotte, J. B. On the universal ac optical background in graphene. *N. J. Phys.* **11**, 095013 (2009).
60. Chen, Z. & Appenzeller, J. in *IEEE International Electron Devices Meeting (IEDM)* 15–17 (San Francisco, USA, 2008).
61. Liu, W., Valdes-Aguilar, R., Hao, Y., Ruoff, R. S. & Armitage, N. P. Broadband microwave and time-domain terahertz spectroscopy of chemical vapor deposition grown graphene. *J. Appl. Phys.* **110**, 083510 (2011).
62. Jablan, M., Buljan, H. & Soljacic, M. Plasmonics in graphene at infrared frequencies. *Phys. Rev. B* **80**, 245435 (2009).
63. Zhu, W., Perebeinos, V., Freitag, M. & Avouris, P. Carrier scattering, mobilities, and electrostatic potential in monolayer, bilayer, and trilayer graphene. *Phys. Rev. B* **80**, 235402 (2009).
64. Adam, S., Hwang, E. H., Galitski, V. M. & Sarma, S. D. A self-consistent theory for graphene transport. *Proc. Natl Acad. Sci.* **10**, 392–397 (2007).
65. Chen, J. H. *et al.* Charged-impurity scattering in graphene. *Nat. Phys.* **4**, 377–381 (2008).
66. Moser, J., Verdaguer, A., Jimenez, D., Barreiro, A. & Bachtold, A. The environment of graphene probed by electrostatic force microscopy. *Appl. Phys. Lett.* **92**, 123507 (2008).
67. Rana, F. Graphene terahertz plasmon oscillators. *IEEE Trans. Nanotechnol.* **7**, 91–99 (2008).

Acknowledgements

This work is dedicated to the memory of Professor Julien Perruisseau-Carrier, of the École Polytechnique Fédérale de Lausanne (Switzerland), who passed away unexpectedly while the manuscript was being prepared for publication. This work was partially supported by the Swiss National Science Foundation (SNSF) under grant 133583, by the European Commission FP7 projects ‘Grafol’ (grant number 133583), Marie-Curie IEF ‘Marconi’ (ref. 300966) and Marie-Curie ITN ‘NAMASEN’, and by Ministerio de Economía y Competitividad, Spain, under grant CONSOLIDER CSD2008-00068.

Author contributions

J.S.G. and J.P.C. conceived the idea of reconfigurable graphene stacks as well as their application in THz plasmonics. J.S.G. developed the theory and analysed the measured data. C.M. and A.I. fabricated the devices. L.S.B. and A.M. grew and transferred the graphene layers. S.C. and J.R. performed the THz measurements. J.S.G. wrote the manuscript (with comments from J.P.C. and S.C.). J.P.C. led the project.

Additional information

Supplementary Information accompanies this paper at <http://www.nature.com/naturecommunications>

Competing financial interests: The authors declare no competing financial interests.

Reprints and permission information is available online at <http://npng.nature.com/reprintsandpermissions/>

How to cite this article: Gomez-Diaz, J. S. *et al.* Self-biased reconfigurable graphene stacks for terahertz plasmonics. *Nat. Commun.* 6:6334 doi: 10.1038/ncomms7334 (2015).